Persistent Photo-Induced Antibacterial Activity of MoS_2 Nanosheets Immobilized in Porous Polymer Beads

*Daehwan Park[a,b], Na Kyung Kim[a], Woo-Ri Shin[c], Chinedum O. Osuji[a]**

[a]Department of Chemical and Biomolecular Engineering, University of Pennsylvania, Philadelphia, Pennsylvania 19104, United States

[b]Department of Chemistry and Cosmetics, Jeju National University, Jeju 63243, Republic of Korea

[c]Department of Bioengineering, University of Pennsylvania, Philadelphia, PA 19104, Unites States

Keywords: two-dimensional (2D) nanomaterial, molybdenum disulfide (MoS_2), reactive oxygen species (ROS), polymer beads, antibacterial effect, reusability

Abstract

Reactive oxygen species (ROS) photogenerated by two-dimensional (2D) nanomaterials provide a means of delivering persistent antibacterial activity in fluid media. Semiconducting molybdenum disulfide (MoS_2) nanosheets are an attractive option for exploiting such activity using visible light.

However, the tendency of MoS_2 nanosheets in suspension to restack or otherwise aggregate remains a critical obstacle as it results in the loss of the desired photo-activity. We report here the development of persistent antibacterial activity by successfully immobilizing MoS_2 nanosheets within porous crosslinked polymer beads. The nanosheet-loaded beads demonstrate continuous antibacterial activity against model species under visible light exposure. The bactericidal activity is associated with ROS-mediated oxidative organismal stress, as assessed through chemical methods using fluorescent probes and gene-level biological studies. The porous beads demonstrate an effective antifouling capability and were physically stable with sustained bactericidal activity at an average of 99 % over 5 cycles. The ability to confer reusable, continuous antibacterial activity under visible light illumination is attractive in the context of the development of sustainable solutions for photoinduced antibacterial materials.

1. Introduction

Disinfection to destroy harmful microorganisms found in drinking water, air, and healthcare settings represents a pressing public health concern.[1, 2] Two-dimensional (2D) nanomaterials, including graphene, carbon nitride, and black phosphorus, have emerged as promising candidates to provide antimicrobial activity due to their photocatalytic properties.[3, 4] They display antibacterial effects through direct and indirect mechanisms. The direct mechanism known as the 'nano-knife effect', involves the physical rupture of cellular structures by the edges of 2D nanomaterials.[5, 6] The efficacy of the direct mechanism is improved by controlling the orientation of the nanomaterial to maximize the presentation of edges[7, 8] but the need for physical interaction constrains the effectiveness overall. By contrast, the indirect mechanism relies on damage by

chemical species generated by the nanomaterial, notably, reactive oxygen species (ROS), which rapidly kill bacteria without prolonged intimate contact.[9] ROS can be generated by semiconducting nanomaterials through redox reactions initiated by absorption of photons with energies exceeding the bandgap.[10,11] Nanomaterials with band gaps in the visible regime, as opposed to the ultra-violet (UV), are most desirable – avoiding the use of UV is beneficial from a safety perspective, while the ability to activate using solar irradiation is attractive in terms of utility.[12, 13]

Among the range of 2D nanomaterials, molybdenum disulfide (MoS_2), stands out as a potential option for antibacterial function. While conventional photocatalyst-based antibacterial materials have relatively high bandgaps that require the use of UV light,[14-16] the narrow direct bandgap of ~1.9 eV in the case of exfoliated MoS_2 nanosheets facilitates the use of visible light.[17-19] In addition, MoS_2 nanosheets can produce ROS with presenting favorable biocompatibility.[20, 21] The biocompatibility of MoS_2 nanosheets stems from their ability to generate ROS in a controlled manner, typically under visible light exposure. This selective ROS production can target and kill bacteria at concentrations effective for antibacterial activity, while minimizing damage to human cells, which possess better antioxidant defense systems.[22] However, the irreversible aggregation tendency of nanosheets often results in a significant reduction in ROS generation efficiency due to the reduction of the key reactive edge sites that are generated during the exfoliation process.[23] Moreover, the multilayer configuration promotes electron-hole recombination between the interlayers, which further hinders ROS formation. To counteract restacking or other aggregation, various supporting materials such as polymers, carbon fiber, and natural rubber have been proposed.[24-26] The photo-induced bactericidal properties of MoS_2 nanosheets in these platforms is noteworthy. However, the lack of persistence of this activity poses a challenge that hinders practical and sustainable applications.

The essence of our study lies in the development of a persistent antibacterial system. To achieve this, MoS_2 nanosheets were immobilized within alginate-based porous polymer beads through a straightforward ionic gelation method. Dispersion of nanosheets within the bead was systematically analyzed through Raman spectroscopy. We further investigated how the nanosheet dispersion impacts photogeneration of ROS and the resulting bactericidal effects. Our hypothesis posits that the bactericidal activity is induced by the ROS-mediated oxidative stress, which was verified by both chemical assays employing fluorescent probes and gene expression-based biological analyses. In particular, the antibacterial mechanism of MoS_2 nanosheets triggered by ROS was explored at the gene level, making this the only study to date to our knowledge. The bead-shaped antibacterial system allows for easy recovery and reuse. The persistence of ROS-induced bactericidal activity was finally demonstrated through multi-cycle antibacterial tests. We strongly anticipate that reusability contributes to the practical and sustainable use of our antibacterial system, highlighting the importance of ROS as a means of achieving persistent bactericidal effects.

2. Experimental Section

2.1. Materials. MoS_2 powder (98 %, < 2 μm), 2.5 M n-butyllithium solution (2.5 M in hexane, 95 %), anhydrous hexane (95 %), a semi-permeable dialysis bag (molecular weight cutoff of 20 kDa), sodium alginate, $CaCl_2$ (> 97 %), glutathione, 5,5′-dithiobis-(2-nitrobenzoic acid (DTNB), and polystyrene (PS, MW = 280,000) were purchased from Sigma. NB broth solution (1×), phosphate buffered saline (PBS), and Tris·HCl buffer (pH 8.3) were purchased from Gibco™. Escherichia coli (*E. coli*, ATCC 25922) was

purchased from ATCC. Tryptic soy broth and LB agar plates were purchased from BD Bacto™ and Moltox, respectively. DCFH-DA staining kit was purchased from Dojindo. QIAGEN RNeasy Mini Kit and Qiagen Reverse Transcription Kit were supplied by QIAGEN. Live/dead assay kit was purchased from Fisher Scientific. Deionized double distilled (DI) water was used for all experiments. All other chemicals were of reagent grade.

2.2. Preparation of MoS_2 nanosheets. MoS_2 nanosheets were prepared via an exfoliation process outlined in the previous work.[27] Specifically, 500 mg of bulk MoS_2 powder (98 %, < 2 μm, Sigma) was added to 2.5 M n-butyllithium solution (2.5 M in hexane, Sigma) at 1 to 3 molar ratio in a nitrogen-filled glovebox (with oxygen and water concentrations maintained below 0.1 ppm), followed by stirring for 2 d under the nitrogen atmosphere. Subsequently, the resulting mixture was washed with anhydrous hexane (95 %, Sigma), and excess n-butyllithium was separated from Li-intercalated MoS_2 through three-times repeated centrifugation at 6000 rpm for 10 min. The fully dried pellet was then diluted in deionized water and bath-sonicated for 1.5 h in an ice bath. After sonication, exfoliated material was exclusively collected from the dark supernatant, separated through twice centrifugation at 2000 rpm for 10 min. The final product was obtained after a 3-d dialysis process in 1 L of deionized water using a semi-permeable dialysis bag (molecular weight cutoff of 20 kDa, Sigma). The concentration of the final MoS_2 suspension was determined by weighing the dried product.

2.3. Fabrication of ABM. A series of ABMs were prepared using MoS_2 nanosheets at different concentrations of 100, 200, and 500 ppm, designated as ABM_{100}, ABM_{200}, and ABM_{500}, correspondingly. Initially, the respective concentration of MoS_2 nanosheets was mixed with 5 wt% sodium alginate (Sigma) solution. The resulting mixture was added dropwise to 5 wt% $CaCl_2$ (> 97 %, Sigma) solution with gentle stirring, maintaining a consistent rate of 0.2 mL/min using a

syringe needle (25 G) coupled with a syringe pump (KD Scientific). The beads were allowed to remain in the solution for 12 h to accomplish the ionic-crosslinking process. Finally, the products were washed with deionized water to remove excess Ca^{2+} ions. For comparison, AB was also prepared using the same procedure but without the incorporation of MoS_2 nanosheets.

2.4. Antibacterial tests. Antibacterial testing was performed, in part, following the procedures of previous studies.[28] A drop of Escherichia coli (*E. coli*, ATCC 25922) suspension in tryptic soy broth (BD Bacto™) solution was streaked on LB agar plates (Moltox), followed by incubation at 37 °C for 12 h. Several colonies were lifted off with a loop, placed in 10 mL of NB broth solution (1×, Gibco™), and incubated with shaking at 37 °C for 12 h. After washing twice with phosphate buffered saline (PBS, Gibco™), the cells were resuspended in PBS to obtain a concentration of 1.5×10^6 colony forming units (CFU)/mL. This value was determined by evaluating the absorbance of the cell dispersion at 600 nm with reference to a standard calibration curve.[29] 5 g of AB, ABM_{100}, ABM_{200}, and ABM_{500} were then introduced to the 10 mL of bacterial solution, respectively, and placed in a custom-made reactor equipped with LED light (120 W, wavelength = 380 to 780 nm). Additionally, a transparent UV blocking film was placed in front of the LED light to block any possible effects of light in the UV range. Each sample was light irradiated for 32 min with stirring at 200 rpm. Every 4 min, 0.1 mL of the solution was taken and added to 0.9 mL of PBS. The resulting solution was serially diluted and then 0.1 mL of each diluent was spread onto the agar plates. The survived *E. coli* colonies were counted after incubating for 18 h at 37 °C. Each test was repeated at least three times. Bacterial survival (%) was calculated according to the equation: Bacterial survival (%) = $100 \times (N_i/N_0)$, where N_0 is the bacterial CFU of the standard sample without any treatment and N_i is the bacterial CFU of the tested sample. For comparison, the same procedure was conducted without any samples under visible light and with samples under

dark conditions. In the reusability test, the same ABM_{200} was used for 5 cycles, being recovered at each cycle, and washed with PBS.

2.5. Bacterial cell morphology analysis. To analyze changes in cell morphology induced by ABM_{200} under visible-light irradiation, the images of the *E. coli* remaining after the antibacterial tests were obtained using scanning electron microscopy (SEM, Quanta 600 FEG ESEM). For the SEM analysis, the cells were fixed according to the protocol described in the previous study.[30] Specifically, cells washed with PBS were immersed in 3 % glutaraldehyde (Sigma) for 10 min at room temperature, followed by dehydration with ethanol. Complete evaporation was ensured prior to analysis. For comparison, the same procedure was repeated for the untreated *E. coli*.

2.6. Detection of ROS generation. Detection of ROS generation was conducted using a DCFH-DA staining kit (Dojindo, Japan). *E. coli* cultured in the same manner as the antibacterial test was stained with the kit and then incubated under dark condition for 30 min. After washing twice with PBS, the cells were resuspended in PBS to obtain a concentration of 1.0×10^8 CFU/mL. 5 g of ABM_{200} was then introduced to the 10 mL of bacterial solution and placed in the custom-made reactor. The same seven samples were exposed to 32 min of visible-light irradiation with stirring at 200 rpm. Samples were collected one by one at 4-min intervals, and the *E. coli* suspension was collected by centrifugation at 6000 rpm for 5 min. The ROS generation was estimated by measuring the fluorescence intensity of DCFH-DA in the *E. coli* samples at 520 nm using a microplate reader (Infinite® M Plex, Tecan, Switzerland).

2.7. Ellman's assay. ROS-mediated oxidative stress was estimated using Ellman's assay. 5 g of ABM_{200} was introduced into a 10 mL mixture solution containing 0.8 mM glutathione (Sigma) in 100 mM bicarbonate buffer (pH 8.6) and allowed to stand for 2 h under dark condition until the glutathione concentration reached saturation due to absorption by the bead. The sample was then

exposed to 32 min of visible-light irradiation with stirring at 200 rpm. Every 4 min, 450 μL of the solution was taken and added to 780 μL of Tris·HCl buffer (pH 8.3, Gibco^{TM}). The resulting solution was treated with 20 μL of 100 mM 5,5′-dithiobis-(2-nitrobenzoic acid) (DTNB, Sigma) solution. Subsequently, the amount of unoxidized glutathione was quantified by measuring the absorbance of the solution at 412 nm. For comparison, the same procedure was repeated for the sample without ABM_{200}. The loss of glutathione (%) was calculated based on the absorbance measurements of the sample under dark conditions.

2.8. RT-qPCR analysis. For real-time RT-qPCR analyses, the residual *E. coli* samples from the ROS detection were subjected to total RNA isolation using the QIAGEN RNeasy Mini Kit (QIAGEN, Germany) according to the manufacturer's instructions. The isolated total RNA was estimated by measuring optical density at 260 nm using NanoDrop ND-1000 Spectrophotometer (Thermo Fisher Scientific, Wilmington, DE). The cDNA was synthesized using the isolated total RNA as a template via Qiagen Reverse Transcription Kit (QIAGEN, Germany). Quantitative Real-time PCR was performed using SYBRgreen Supermix (Bio-rad, Hercules, CA). Analysis of the synthesized cDNA levels was carried out in triplicate in Real Time-PCR 7300 (Applied Biosystems, USA) using specific primers (**Table S1**).[31]

2.9. Antifouling tests. To obtain the clear microscope image, ABM_{200} was prepared in a film form rather than a bead shape, by spin-coating the 200 ppm mixture solution of MoS_2 nanosheets suspension in 5 wt% sodium alginate solution on the silicon wafer substrate at 1500 rpm for 2 min. Subsequently, the film was immersed in a $CaCl_2$ solution for ionic crosslinking. *E. coli* (1.0×10^8 CFU/mL) was incubated on the film at room temperature for 10 h, then stained with a live/dead assay kit (Fisher Scientific) following the manufacturer's guidelines. The resulting film was gently rinsed three times with PBS. Microscope images were captured at each rinse using a laser scanning

confocal microscope (LSM 800, Carl Zeiss). The count of *E. coli* attached to the film was determined using ImageJ software. The same procedure was replicated for PS (MW = 280,000, Sigma) coated film as a negative control.

2.10. Material Characterization. The morphology of the MoS_2 nanosheet was observed with a transmission electron microscope (TEM, JEM-F200 F2, JEOL, USA) operating at 200 kV. The thickness of the MoS_2 nanosheet was measured from an atomic force microscope (AFM, Dimension Icon, Bruker, USA) image. Raman spectra were obtained from a LabRam Evolution confocal Raman microscope (HORIBA, France), using 633 nm light excitation and 300 s exposure under a 100× objective. Thermogravimetric analysis (TGA) was carried out using an SDT Q650 (TA Instruments, USA) at a scan rate of 10 °C/min. The water contact angle image was captured using a USB camera, and the measurement was conducted using ImageJ software.

3. Results and Discussion

3.1. Fabrication of Porous Beads

Figure 1a illustrates the fabrication procedure of the MoS_2 nanosheets-immobilized alginate-based porous bead (ABM) using an ionic-gelation method.[32] As the first step, MoS_2 nanosheets were prepared through the exfoliation of bulk MoS_2 with lithium intercalation.[27] Based on transmission electron microscopy (TEM) and atomic force microscopy (AFM) analyses, the width of the nanosheets varied from 50 to 300 nm, with an average width of 147 nm and an average thickness of 1.0 nm (±0.2 nm), respectively (**Figure 1b-d**). The thickness measurement suggests that the MoS_2 nanosheets suspension mainly consists of single and few-layer nanosheets. The MoS_2 nanosheets were homogeneously mixed with sodium alginate solution, and then added to a

calcium chloride ($CaCl_2$) solution using a syringe pump, yielding uniformly sized beads (radius = 1.35 mm, **Figure 1e**). The formation of the bead structure is facilitated by the 'egg box'-like ionic crosslinking arrangement, wherein the positively charged calcium ions (Ca^{2+}) interlock with the spaces between the elongated, negatively charged alginate chains.[33] Through the ionic gelation process, the MoS_2 nanosheets can be physically anchored within the cross-linked 3D networks of alginate (**Figure 1f**). To determine the optimal condition for the uniform dispersion of MoS_2 nanosheets within the bead, the MoS_2 concentration in the mixture solution was further controlled to 100, 200, and 500 ppm, and the corresponding ABMs were designated as ABM_{100}, ABM_{200}, and ABM_{500}, respectively (**Figure S1**). Alginate beads (ABs) without MoS_2 were also prepared for comparison. The dispersion of MoS_2 within the bead can be assessed through the wavenumber difference (Δk) between the two distinct vibrational modes,[34] E^1_{2g} and A_{1g}, in the Raman spectrum (**Figure 1g)**. The Δk value was approximately 22.28 cm^{-1} for ABM_{100}, 22.30 cm^{-1} for AMB_{200}, and 25.16 cm^{-1} for ABM_{500}. The Δk value of ABM_{500} is close to that of bulk MoS_2 (Δk = 26.95 cm^{-1}) in contrast to the values of ABM_{100} and ABM_{200}, which means that there exists a limiting capacity for nanosheets to be uniformly dispersed within the beads. Therefore, 200 ppm was found to be the optimal MoS_2 concentration to maintain the uniform dispersion of nanosheets without significant restacking.

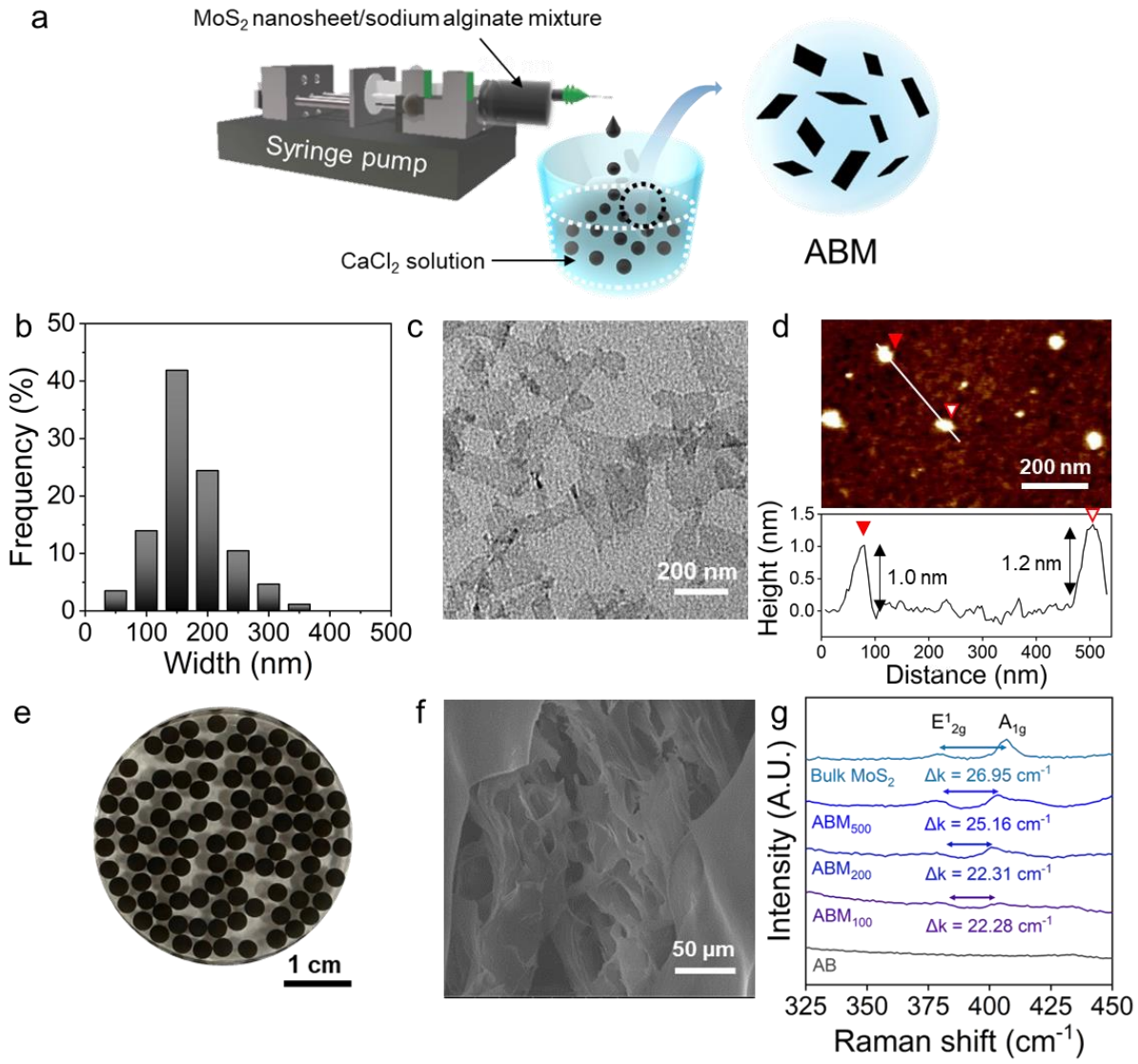

Figure 1. a) Schematic illustration of the fabrication procedure of MoS_2 nanosheet-immobilized alginate-based porous beads (ABM). b) Lateral size distribution of MoS_2 nanosheets observed in c) the representative TEM image of MoS_2 nanosheets. The inset in d) AFM image of MoS_2 nanosheets shows the height profile along the white line. e) A photo and f) cross-section SEM image of ABM_{200}. g) Raman spectrum of AB, ABM_{100}, ABM_{200}, ABM_{500}, and bulk MoS_2.

3.2. Visible light-induced bactericidal activity of ABM

The influence of visible-light irradiation and MoS_2 concentration on the ROS-induced bactericidal effect of ABM was systematically investigated using a custom-made reactor (**Figure S2**). In the absence of light irradiation, neither AB nor ABM_{200} exhibit significant bactericidal properties (**Figure S3**). Under visible light, only ABM_{200} exhibited significant bactericidal effect, demonstrating the highest efficacy. ABM_{200} rendered over 80% of *E. coli* within 16 min and over 97% within 32 min (**Figures 2a** and **2b**). The bactericidal effect was further evidenced by morphological changes of the bacteria, including flattening and cell rupture, which are recognized as indicators of cell death (**Figure 2c and 2d**).[35] The photo-induced bactericidal activity of ABM_{200} surpasses that of both ABM_{100} and ABM_{500} (**Figure S4**), in accordance with the tendency observed in the uniform dispersion of MoS_2 nanosheets. These combined quantitative and qualitative findings underscore that substantial bactericidal activity is achievable when uniform dispersion of a maximum amount of MoS_2 nanosheets can be ensured. In addition, the size of ABM and visible-light intensity affect the ROS generation efficiency, which further influences the antibacterial performance. Further studies are needed in this regard.

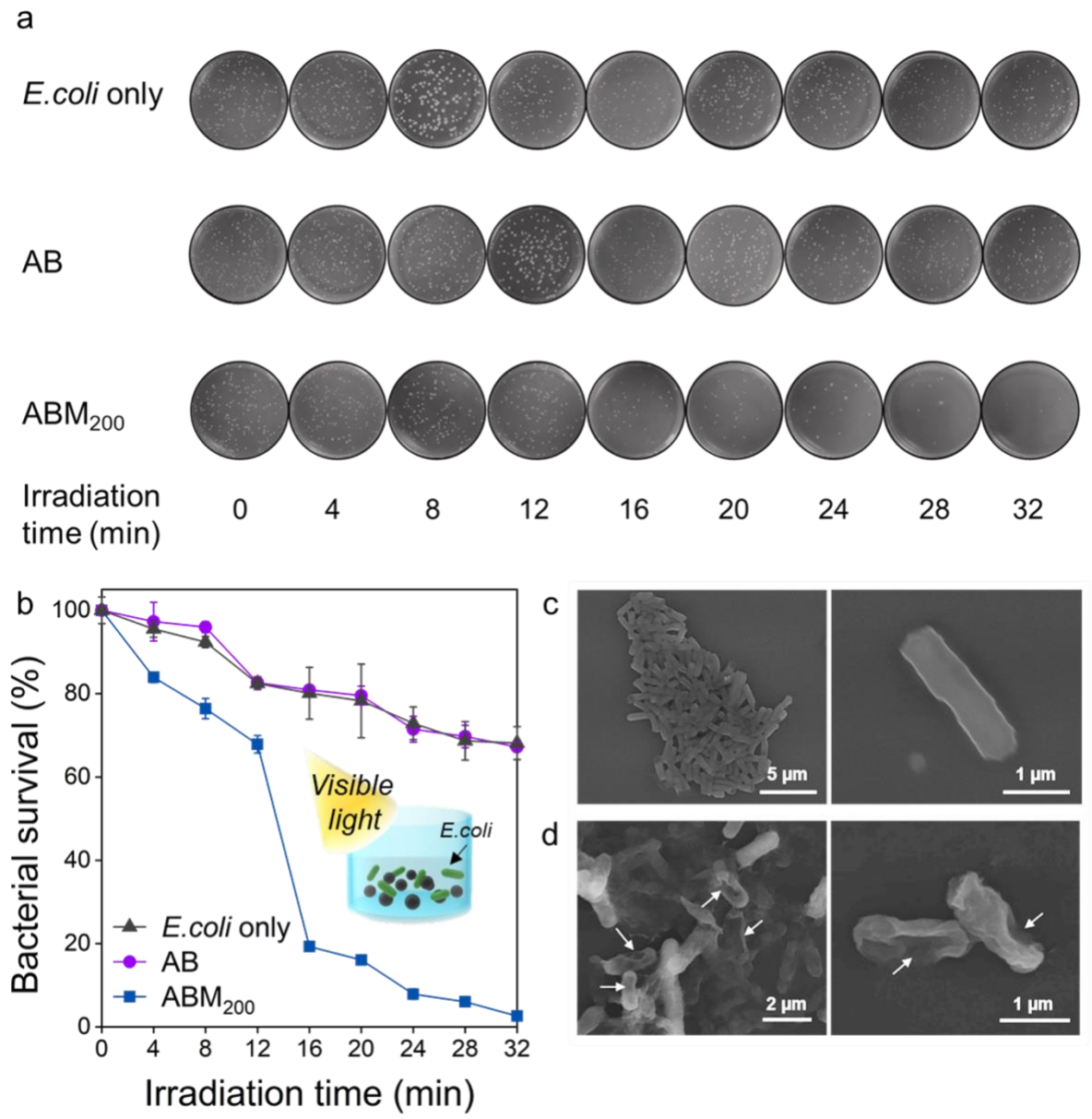

Figure 2. a) Photographic results of bacterial survival obtained from only *E. coli* solution and the solution treated with AB, and ABM_{200}, respectively, under visible-light irradiation at 4 min intervals for a total of 32 min, and b) corresponding quantitative data. SEM images of *E. coli* exposed to ABM_{200} under c) dark and d) visible light irradiation for 32 min, respectively. The SEM image on the right side of c) and d) is an enlarged view. The arrow indicates the photo-induced morphological changes of *E. coli.*

3.3. Chemical assays to verify ROS generation

Figure 3a illustrates the bactericidal effects induced by photogenerated ROS in the ABM system. MoS_2 nanosheets absorb photons and generate electron (e_{CB}^-) - hole (h_{VB}^+) pairs. The excited-state electrons then initiate a reaction with molecular oxygen to produce superoxide radicals ($^{\bullet}O_2^-$), leading to a sequence of redox reactions that yield other ROS, such as H_2O_2 and $^{\bullet}OH$, shown in sequences (1) to (4). The induced holes (h_{VB}^+) also react with water molecule to form hydroxyl radicals (5): [36, 37]

$$MoS_2 + h\nu \rightarrow e_{CB}^- + h_{VB}^+ \quad (1)$$

$$O_2 + e^- \rightarrow {}^{\bullet}O_2^- \quad (2)$$

$$^{\bullet}O_2^- + H^+ \rightarrow H_2O_2 \quad (3)$$

$$H_2O_2 + h\nu \rightarrow 2\ {}^{\bullet}OH \quad (4)$$

$$H_2O + h_{VB}^+ \rightarrow {}^{\bullet}OH \quad (5)$$

These ROS generating reactions primarily take place at the edges of MoS_2 nanosheets, particularly at defects created during the exfoliation process.[38] This highlights the importance of the uniform dispersion of nanosheets in providing more reaction sites for ROS generation. We first verified the generation of ROS in the ABM system under visible-light irradiation via a chemical study using a highly sensitive fluorescent probe, 2',7'-dichlorofluorescin diacetate (DCFH-DA). DCFH-DA selectively detects ROS that reach *E. coli* by undergoing the process (5) within the cellular environment.[39]

$$\text{DCFH-DA} \xrightarrow{hydrolysis} \text{DCFH} \xrightarrow{oxidation} \text{DCF} \quad (5)$$

DCFH-DA is hydrolyzed by esterase within *E. coli* to produce 2',7'-dichlorofluorescin (DCFH), which can be oxidized by ROS to form the highly fluorescent 2',7'-dichlorofluorescein (DCF). As shown in **Figure 3b**, the fluorescence intensity gradually increases until the final level accumulated over 32 min exceeds 66.2 % of the initial level. This result suggests that ROS are readily delivered to *E. coli* without significant interference by the beads.

We confirmed the onset of ROS-mediated oxidative stress using Ellman's assay.[40] Glutathione (GSH) is used as a model compound since it is commonly found in most Gram-negative bacteria and its oxidation into glutathione disulfide (GSSG) by ROS is closely linked to cell death.[41] By monitoring the color change from yellow (GSH) to colorless (GSSG) based on optical absorbance at 420 nm, the extent of ROS-mediated oxidative stress can be indirectly estimated. Exposure to ABM_{200} with visible light results in 93 % depletion of GSH within 16 min, ultimately leading to complete loss of absorbance after 32 min (**Figure 3c**). This rapid oxidation of GSH into GSSG is consistent with the trend observed in the earlier antibacterial test results, thus demonstrating that photogenerated ROS can induce oxidative stress for effective bacterial inactivation.

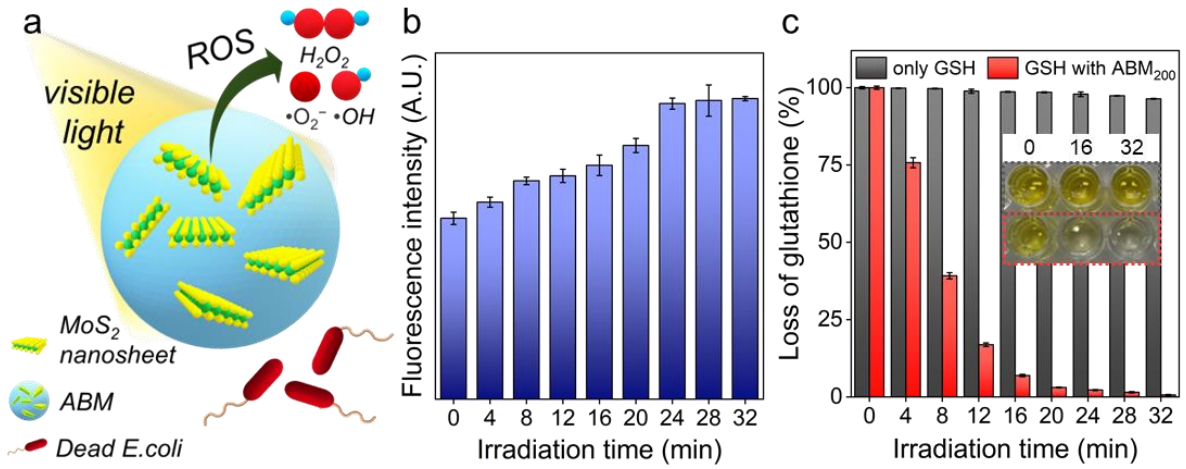

Figure 3. a) Schematic diagram of the bactericidal effects induced by ROS photogenerated in the ABM system. b) Fluorescence intensity of DCF measured at 512 nm for detection of ROS generation. c) Loss of glutathione (%) calculated based on the absorbance of GSH at 420 nm for assessment of ROS-mediated oxidative stress. Both b) and c) were monitored at 4 min intervals over a total visible-light irradiation time of 32 min. The inset photo in c) represents the color change of GSH solution at 0, 16, and 32 min of visible-light irradiation without (top layer) and with (bottom layer) ABM_{200}.

3.4. Biological studies on antibacterial mechanism induced by ROS

We further investigated how ROS-mediated oxidative stress damages *E. coli* by analyzing gene expression under ROS-sensing transcriptional regulons, including soxR, soxS, and oxyR. These regulons serve as defense systems for *E. coli*, regulating the transcription of various genes involved in the response to elevated ROS levels. Thus, monitoring the respective mRNA levels can enhance our understanding of the antibacterial mechanism triggered by ROS. **Figures 4a** and **4b** show the increase in soxR/S and oxyR, demonstrating that *E. coli* promptly activates the defense mechanism in response to the photo-induced ROS generation in the ABM system. The defense mechanism involves gene expression of sodA, zwf, and fumC induced by soxR/S and katG, ahpC, dps, and grxC activated by oxyR, respectively.[42, 43] For some genes, such as ahpC and grxC, the expression

level did not increase linearly over time. This is because continuous damage may temporarily decrease intracellular oxidative stress or activate cellular pathways that downregulate expression.[31, 44] However, the mRNA levels for most genes consistently increase over a 32 min light irradiation period, reaching 2- to 6-fold of the initial levels. **Figure 4c** illustrates the subsequent protein encoding resulting from the gene expression, helping ROS management. For example, sodA, katG, and ahpC assist *E. coli* in alleviating oxidative stress by decomposing ROS into less toxic molecular substances. Additionally, dps and grxC play crucial roles in DNA protection and repair of oxidatively damaged cellular proteins, respectively. Furthermore, zwf and fumC contribute to restoring cellular metabolism and redox balance. This comprehensive gene expression analysis provides strong evidence that oxidative stress damage occurs through various pathways, affecting DNA, proteins, metabolic processes, and redox system. To the best of our knowledge, this study represents the first comprehensive gene-level analysis of the antibacterial mechanism of ROS based on MoS_2 nanosheets.

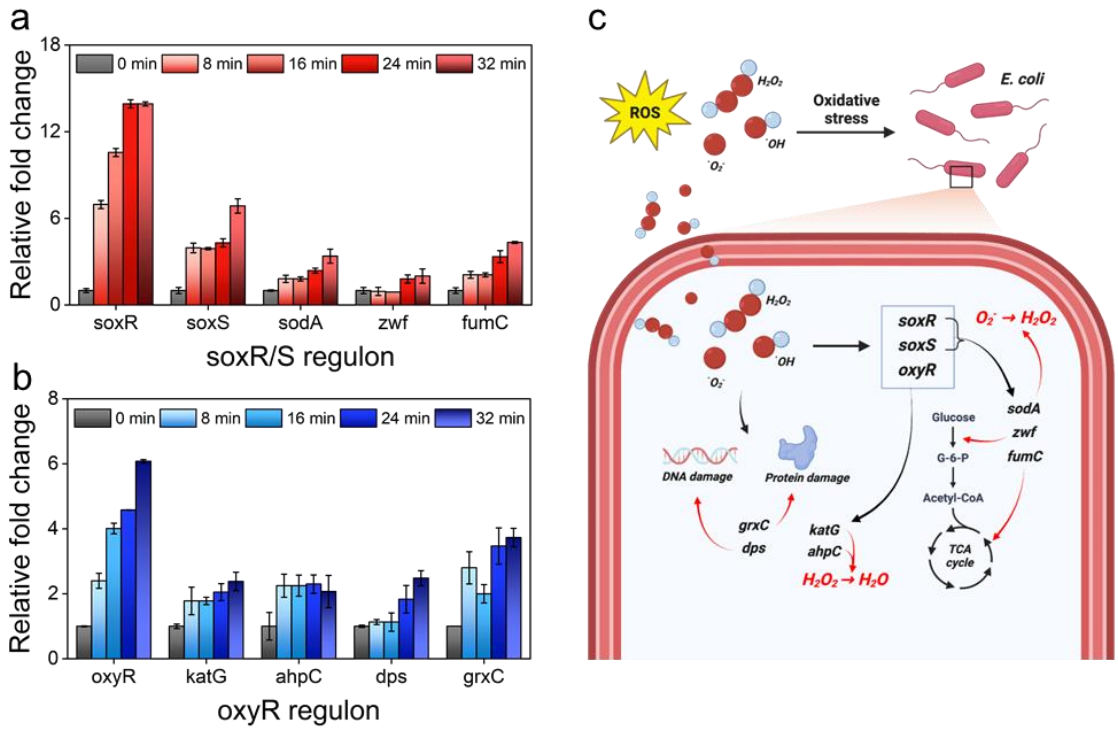

Figure 4. Time course gene expression activated by a) soxR and soxS and b) oxyR in the ABM system under visible-light irradiation, with detection intervals of 8 min for a total of 32 min. c) Schematic diagram illustrating the gene expression regulated by soxR/S and oxyR in response to oxidative stress in *E. coli*, along with the respective protein encoding.

3.5. Persistent bactericidal activity in reusable ABM system

The reusability of the system, and therefore the persistence of the ROS-induced bactericidal activity, were demonstrated through multi-cycle testing. A sample of ABM_{200} was subjected to 5 cycles of testing. The sample exhibited an average bactericidal activity of 99 % over the 5 cycles (**Figure 5a**). In addition, the recovered beads maintained their physical integrity and MoS_2 nanosheets loading, as reflected by the consistent char yield of 40 % over 5 cycles (**Figure 5b**). The consistency of the bactericidal activity suggests that there is no significant biofouling of the beads – biofouling associated with the growth of a biofilm would be expected to suppress the bactericidal activity. We speculate that the hydrophilic nature of the beads may act to inhibit biofouling.[45, 46] As shown in **Figure 5c-e,** only a few *E. coli* were observed adhered on the hydrophilic ABM_{200} surface (water contact angle, WCA = 13.5 ^{o}), while the hydrophobic polystyrene (PS) surface (WCA =90.9 ^{o}) remains densely covered with over 700 bacterial cells even after three rinses. The results overall indicate that the ABM are effective materials for achieving persistent visible light-induced antibacterial activity, and indeed their performance compares favorably against prior reported examples (**Table S2**).[47-56] We anticipate that the materials demonstrated here may be of interest for a variety of applications, including water treatment and disease prevention.

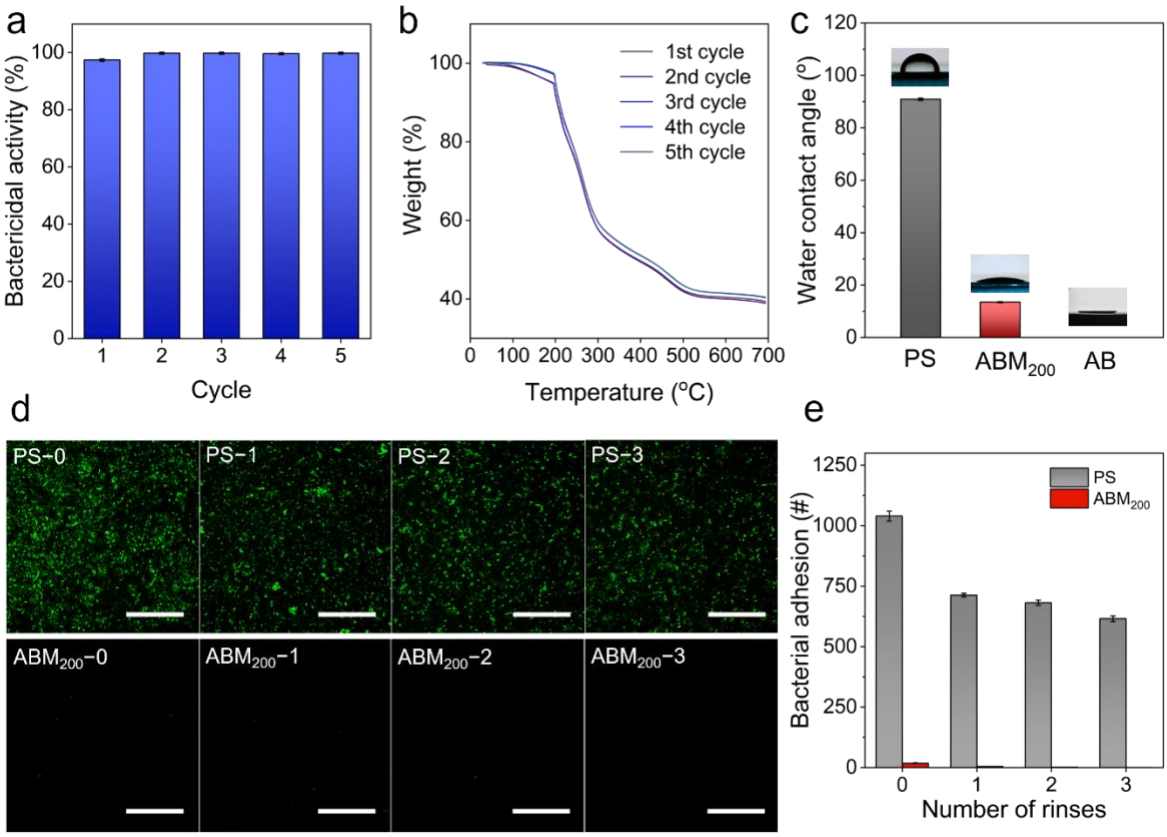

Figure 5. a) The bactericidal activity (%) obtained by repeated use of ABM_{200} for 5 cycles of visible-light irradiation for 32 min each. b) TGA thermograms of ABM_{200} obtained at each cycle from the 1st to the 5th cycle of antibacterial tests. c) Water contact angles measured on the surfaces of PS and ABM_{200}, and AB with corresponding representative photos on top of each column. d) Representative fluorescence microscope images and e) the number of adhered *E. coli* on the surface of PS and ABM_{200}, respectively. The images were taken before and after 1 to 3 times-rinsing with PBS to remove the loosely attached *E. coli* (scale bar = 50 um).

4. Conclusion

In summary, we successfully developed a persistent antibacterial system by immobilizing exfoliated MoS_2 nanosheets within alginate-based polymer beads using a simple ionic-gelation method. The dispersion of the optimal amount of nanosheets within the bead platform guaranteed

substantial ROS generation under visible light, resulting in robust bactericidal effects. Chemical studies systematically assessed the ROS-mediated oxidative stress, identifying this process as a fundamental source of bactericidal activity. Further biological analysis revealed alterations in gene expression levels within *E. coli* as part of their adaptive response to oxidative stress. This information has proven invaluable in understanding cellular pathways that elucidate how ROS affect DNA, proteins, metabolic processes, and redox balance in *E. coli*. Finally, we demonstrated the persistence of our bead system, showcasing an average bactericidal activity of 99 % over 5 cycles. This reusability significantly enhances the practical application and sustainability of photoinduced antibacterial materials. We believe our material holds strong potential for applications such as portable water purification and wound healing patches. Future research will focus on optimizing synthesis for scalability, enhancing ROS production under varied light conditions, and improving skin adhesion for effective biocompatible wound care.

ASSOCIATED CONTENT

Supporting Information.

More information and details about the real image of ABM, photoreactor, comparative table, and primers for RT-qPCR (PDF)

AUTHOR INFORMATION

Corresponding Author

*E-mail: cosuji@seas.upenn.edu (C. O. Osuji)

Author Contributions

D. Park and N. K. Kim contributed equally to this work. All authors have given approval to the final version of the manuscript.

ACKNOWLEDGMENT

The authors acknowledge financial support from the Center for Engineering MechanoBiology (CEMB) under the National Science Foundation (NSF) grant number CMMI: 1548571 at the University of Pennsylvania. C.O.O. acknowledges additional NSF support through DMR 2223705.

REFERENCES

(1) Feng, X.; Imran, Q.; Zhang, Y.; Sixdenier, L.; Lu, X.; Kaufman, G.; Gabinet, U.; Kawabata, K.; Elimelech, M.; Osuji, C. O. Precise nanofiltration in a fouling-resistant self-assembled membrane with water-continuous transport pathways. *Sci. Adv.* **2019**, *5* (8), eaav9308. DOI: doi:10.1126/sciadv.aav9308
(2) Zhang, X.; Wu, J.; Smith, L. M.; Li, X.; Yancey, O.; Franzblau, A.; Dvonch, J. T.; Xi, C.; Neitzel, R. L. Monitoring SARS-CoV-2 in air and on surfaces and estimating infection risk in buildings and buses on a university campus. *J. Expo. Sci. Environ. Epidemiol.* **2022**, *32* (5), 751-758. DOI: 10.1038/s41370-022-00442-9
(3) Shaw, Z. L.; Kuriakose, S.; Cheeseman, S.; Dickey, M. D.; Genzer, J.; Christofferson, A. J.; Crawford, R. J.; McConville, C. F.; Chapman, J.; Truong, V. K.; et al. Antipathogenic properties and applications of low-dimensional materials. *Nat. Commun.* **2021**, *12* (1), 3897. DOI: 10.1038/s41467-021-23278-7
(4) Gokce, C.; Gurcan, C.; Besbinar, O.; Unal, M. A.; Yilmazer, A. Emerging 2D materials for antimicrobial applications in the pre- and post-pandemic era. *Nanoscale* **2022**, *14* (2), 239-249. DOI: 10.1039/d1nr06476b
(5) Ravichandran, G.; Yadav, D. N.; Murugappan, S.; Sankaranarayanan, S. A.; Revi, N.; Rengan, A. K. "Nano effects": a review on nanoparticle-induced multifarious systemic effects on cancer theranostic applications. *Mater. Adv.* **2022**, *3* (22), 8001-8011. DOI: 10.1039/d2ma00784c
(6) Li, Y.; Yuan, H.; von dem Bussche, A.; Creighton, M.; Hurt, R. H.; Kane, A. B.; Gao, H. Graphene microsheets enter cells through spontaneous membrane penetration at edge asperities and corner sites. *Proc. Natl. Acad. Sci.* **2013**, *110* (30), 12295-12300. DOI: 10.1073/pnas.1222276110
(7) Virgo, E. P.; Haidari, H.; Shaw, Z. L.; Huang, L. Z. Y.; Kennewell, T. L.; Smith, L.; Ahmed, T.; Bryant, S. J.; Howarth, G. S.; Walia, S.; et al. Layered Black Phosphorus Nanoflakes Reduce Bacterial Burden and Enhance Healing of Murine Infected Wounds. *Adv. Therap.* **2023**. DOI: 10.1002/adtp.202300235

(8) Lu, X.; Feng, X.; Werber, J. R.; Chu, C.; Zucker, I.; Kim, J.-H.; Osuji, C. O.; Elimelech, M. Enhanced antibacterial activity through the controlled alignment of graphene oxide nanosheets. *Proc. Natl. Acad. Sci.* **2017**, *114* (46), E9793-E9801. DOI: doi:10.1073/pnas.1710996114
(9) Yu, Y.; Lu, L.; Yang, Q.; Zupanic, A.; Xu, Q.; Jiang, L. Using MoS_2 Nanomaterials to Generate or Remove Reactive Oxygen Species: A Review. *ACS Appl. Nano Mater.* **2021**, *4* (8), 7523-7537. DOI: 10.1021/acsanm.1c00751
(10) Liu, C.; Kong, D.; Hsu, P.-C.; Yuan, H.; Lee, H.-W.; Liu, Y.; Wang, H.; Wang, S.; Yan, K.; Lin, D. Rapid water disinfection using vertically aligned MoS_2 nanofilms and visible light. *Nat. Nanotechnol.* **2016**, *11* (12), 1098-1104.
(11) Huang, Y.; Guo, J.; Li, Y.; Li, H.; Fan, D. E. 2D-Material-Integrated Micromachines: Competing Propulsion Strategy and Enhanced Bacterial Disinfection. *Adv. Mater.* **2022**, *34* (30), e2203082. DOI: 10.1002/adma.202203082
(12) Lee, K.; Shin, S.; Lee, W. J.; Choi, D.; Ahn, Y.; Park, M.; Seo, D.; Seo, K. Sunlight-Activatable ROS Generator for Cell Death Using TiO_2/*c*-Si Microwires. *Nano Lett.* **2021**, *21* (16), 6998-7004. DOI: 10.1021/acs.nanolett.1c02337
(13) Marín-Caba, L.; Bodelón, G.; Negrín-Montecelo, Y.; Correa-Duarte, M. A. Sunlight-Sensitive Plasmonic Nanostructured Composites as Photocatalytic Coating with Antibacterial Properties. *Adv. Funct. Mater.* **2021**, *31* (46). DOI: 10.1002/adfm.202105807
(14) Azizi-Lalabadi, M.; Ehsani, A.; Divband, B.; Alizadeh-Sani, M. Antimicrobial activity of Titanium dioxide and Zinc oxide nanoparticles supported in 4A zeolite and evaluation the morphological characteristic. *Sci. Rep.* **2019**, *9* (1), 17439. DOI: 10.1038/s41598-019-54025-0
(15) Nagay, B. E.; Dini, C.; Cordeiro, J. M.; Ricomini-Filho, A. P.; de Avila, E. D.; Rangel, E. C.; da Cruz, N. C.; Barao, V. A. R. Visible-Light-Induced Photocatalytic and Antibacterial Activity of TiO_2 Codoped with Nitrogen and Bismuth: New Perspectives to Control Implant-Biofilm-Related Diseases. *ACS Appl. Mater. Interfaces* **2019**, *11* (20), 18186-18202. DOI: 10.1021/acsami.9b03311
(16) Aldeen, T. S.; Ahmed Mohamed, H. E.; Maaza, M. ZnO nanoparticles prepared via a green synthesis approach: Physical properties, photocatalytic and antibacterial activity. *J. Phys. Chem. Solids* **2022**, *160*. DOI: 10.1016/j.jpcs.2021.110313
(17) Venkata Subbaiah, Y. P.; Saji, K. J.; Tiwari, A. Atomically Thin MoS_2: A Versatile Nongraphene 2D Material. *Adv. Funct. Mater.* **2016**, *26* (13), 2046-2069. DOI: 10.1002/adfm.201504202
(18) Parzinger, E.; Miller, B.; Blaschke, B.; Garrido, J. A.; Ager, J. W.; Holleitner, A.; Wurstbauer, U. Photocatalytic stability of single-and few-layer MoS_2. *ACS Nano* **2015**, *9* (11), 11302-11309.
(19) Li, H.; Zhang, Q.; Yap, C. C. R.; Tay, B. K.; Edwin, T. H. T.; Olivier, A.; Baillargeat, D. From Bulk to Monolayer MoS_2: Evolution of Raman Scattering. *Adv. Funct. Mater.* **2012**, *22* (7), 1385-1390. DOI: 10.1002/adfm.201102111
(20) Appel, J. H.; Li, D. O.; Podlevsky, J. D.; Debnath, A.; Green, A. A.; Wang, Q. H.; Chae, J. Low Cytotoxicity and Genotoxicity of Two-Dimensional MoS_2 and WS_2. *ACS Biomater. Sci. Eng.* **2016**, *2* (3), 361-367. DOI: 10.1021/acsbiomaterials.5b00467
(21) Kaur, J.; Singh, M.; Dell'Aversana, C.; Benedetti, R.; Giardina, P.; Rossi, M.; Valadan, M.; Vergara, A.; Cutarelli, A.; Montone, A. M. I.; et al. Biological interactions of biocompatible and water-dispersed MoS_2 nanosheets with bacteria and human cells. *Sci. Rep.* **2018**, *8* (1), 16386. DOI: 10.1038/s41598-018-34679-y

(22) Wang, H.; Xia, P.; Kurboniyon, M. S.; Fang, S.; Huang, K.; Ning, S.; Jin, G.; Zhang, L.; Wang, C. V-doped MoS_2 nanozymes providing reactive oxygen species and depleting glutathione for photothermally-enhanced nanocatalytic therapy. *Front Pharmacol.* **2024**, *15*, 1448867. DOI: 10.3389/fphar.2024.1448867
(23) Kibsgaard, J.; Chen, Z.; Reinecke, B. N.; Jaramillo, T. F. Engineering the surface structure of MoS_2 to preferentially expose active edge sites for electrocatalysis. *Nat. Mater.* **2012**, *11* (11), 963-969.
(24) Remanan, S.; Padmavathy, N.; Rabiya, R.; Ghosh, S.; Das, T. K.; Bose, S.; Sen, R.; Das, N. C. Converting Polymer Trash into Treasure: An Approach to Prepare MoS_2 Nanosheets Decorated PVDF Sponge for Oil/Water Separation and Antibacterial Applications. *Ind. Eng. Chem. Res.* **2020**, *59* (45), 20141-20154. DOI: 10.1021/acs.iecr.0c03069
(25) Tang, Y.; Qin, Z.; Zhong, Y.; Yan, X.; Kong, L.; Yang, X.; Yin, S.; Li, M.; Liu, Z.; Sun, H. Bioinspired MoS_2 Nanosheet-Modified Carbon Fibers for Synergetic Bacterial Elimination and Wound Disinfection. *Adv. Healthc. Mater.* **2023**, *12* (8), e2202270. DOI: 10.1002/adhm.202202270
(26) Sethulekshmi, A. S.; Saritha, A.; Joseph, K.; Aprem, A. S.; Sisupal, S. B.; Nair, V. S.; G, S. Multifunctional role of tannic acid in improving the mechanical, thermal and antimicrobial properties of natural rubber-molybdenum disulfide nanocomposites. *Int. J. Biol. Macromol.* **2023**, *225*, 351-360. DOI: 10.1016/j.ijbiomac.2022.11.054
(27) Lu, X.; Gabinet, U. R.; Ritt, C. L.; Feng, X.; Deshmukh, A.; Kawabata, K.; Kaneda, M.; Hashmi, S. M.; Osuji, C. O.; Elimelech, M. Relating Selectivity and Separation Performance of Lamellar Two-Dimensional Molybdenum Disulfide (MoS_2) Membranes to Nanosheet Stacking Behavior. *Environ. Sci. Technol.* **2020**, *54* (15), 9640-9651. DOI: 10.1021/acs.est.0c02364
(28) Choi, Y.-S.; Kim, N. K.; Kang, H.; Jang, H.-K.; Noh, M.; Kim, J.; Shon, D.-J.; Kim, B.-S.; Lee, J.-C. Antibacterial and biocompatible ABA-triblock copolymers containing perfluoropolyether and plant-based cardanol for versatile coating applications. *RSC Adv.* **2017**, *7* (60), 38091-38099. DOI: 10.1039/c7ra07689d
(29) Bordenave, N.; Grelier, S.; Coma, V. Hydrophobization and antimicrobial activity of chitosan and paper-based packaging material. *Biomacromolecules* **2010**, *11* (1), 88-96.
(30) Kim, N. K.; Cha, E. J.; Jung, M.; Kim, J.; Jeong, G.-J.; Kim, Y. S.; Choi, W. J.; Kim, B.-S.; Kim, D.-G.; Lee, J.-C. 3D hierarchical scaffolds enabled by a post-patternable, reconfigurable, and biocompatible 2D vitrimer film for tissue engineering applications. *J. Mater. Chem. B* **2019**, *7* (21), 3341-3345. DOI: 10.1039/c9tb00221a
(31) Baez, A.; Shiloach, J. Escherichia coli avoids high dissolved oxygen stress by activation of SoxRS and manganese-superoxide dismutase. *Microb. Cell Fact.* **2013**, *12*, 23.
(32) Ji, D.; Park, J. M.; Oh, M. S.; Nguyen, T. L.; Shin, H.; Kim, J. S.; Kim, D.; Park, H. S.; Kim, J. Superstrong, superstiff, and conductive alginate hydrogels. *Nat. Commun.* **2022**, *13* (1), 3019. DOI: 10.1038/s41467-022-30691-z
(33) Tan, L. L.; Mahotra, M.; Chan, S. Y.; Loo, S. C. J. In situ alginate crosslinking during spray-drying of lactobacilli probiotics promotes gastrointestinal-targeted delivery. *Carbohydr. Polym.* **2022**, *286*, 119279. DOI: 10.1016/j.carbpol.2022.119279
(34) Gabinet, U. R.; Lee, C.; Poling-Skutvik, R.; Keane, D.; Kim, N. K.; Dong, R.; Vicars, Z.; Cai, Y.; Thosar, A. U.; Grun, A.; et al. Nanocomposites of 2D-MoS_2 Exfoliated in Thermotropic Liquid Crystals. *ACS Mater.Lett.* **2021**, *3* (6), 704-712. DOI: 10.1021/acsmaterialslett.1c00222

(35) Liu, P.; Wu, Y.; Mehrjou, B.; Tang, K.; Wang, G.; Chu, P. K. Versatile Phenol-Incorporated Nanoframes for In Situ Antibacterial Activity Based on Oxidative and Physical Damages. *Adv. Funct. Mater.* **2022**, *32* (17). DOI: 10.1002/adfm.202110635
(36) Cheng, P.; Zhou, Q.; Hu, X.; Su, S.; Wang, X.; Jin, M.; Shui, L.; Gao, X.; Guan, Y.; Nozel, R.; et al. Transparent Glass with the Growth of Pyramid-Type MoS_2 for Highly Efficient Water Disinfection under Visible-Light Irradiation. *ACS Appl. Mater. Interfaces* **2018**, *10* (28), 23444-23450. DOI: 10.1021/acsami.8b06656
(37) Liu, C.; Kong, D.; Hsu, P. C.; Yuan, H.; Lee, H. W.; Liu, Y.; Wang, H.; Wang, S.; Yan, K.; Lin, D.; et al. Rapid water disinfection using vertically aligned MoS_2 nanofilms and visible light. *Nat. Nanotechnol.* **2016**, *11* (12), 1098-1104. DOI: 10.1038/nnano.2016.138
(38) Yang, X.; Li, J.; Liang, T.; Ma, C.; Zhang, Y.; Chen, H.; Hanagata, N.; Su, H.; Xu, M. Antibacterial activity of two-dimensional MoS_2 sheets. *Nanoscale* **2014**, *6* (17), 10126-10133.
(39) Gao, Q.; Zhang, X.; Yin, W.; Ma, D.; Xie, C.; Zheng, L.; Dong, X.; Mei, L.; Yu, J.; Wang, C.; et al. Functionalized MoS_2 Nanovehicle with Near-Infrared Laser-Mediated Nitric Oxide Release and Photothermal Activities for Advanced Bacteria-Infected Wound Therapy. *Small* **2018**, *14* (45), e1802290. DOI: 10.1002/smll.201802290
(40) Vecitis, C. D.; Zodrow, K. R.; Kang, S.; Elimelech, M. Electronic-structure-dependent bacterial cytotoxicity of single-walled carbon nanotubes. *ACS Nano* **2010**, *4* (9), 5471-5479.
(41) Zhou, X.; Zhang, S.; Liu, Y.; Meng, J.; Wang, M.; Sun, Y.; Xia, L.; He, Z.; Hu, W.; Ren, L.; et al. Antibacterial Cascade Catalytic Glutathione-Depleting MOF Nanoreactors. *ACS Appl. Mater. Interfaces* **2022**, *14* (9), 11104-11115. DOI: 10.1021/acsami.1c24231
(42) Li, Z.; Demple, B. SoxS, an activator of superoxide stress genes in Escherichia coli. Purification and interaction with DNA. *J. Biol. Chem.* **1994**, *269* (28), 18371-18377.
(43) Wan, F.; Shi, M.; Gao, H. Loss of OxyR reduces efficacy of oxygen respiration in Shewanella oneidensis. *Sci. Rep.* **2017**, *7* (1), 42609.
(44) Roth, M.; Jaquet, V.; Lemeille, S.; Bonetti, E. J.; Cambet, Y.; Francois, P.; Krause, K. H. Transcriptomic Analysis of E. coli after Exposure to a Sublethal Concentration of Hydrogen Peroxide Revealed a Coordinated Up-Regulation of the Cysteine Biosynthesis Pathway. *Antioxidants* **2022**, *11* (4). DOI: 10.3390/antiox11040655
(45) Kim, N. K.; Kim, J.; Shon, D.-J.; Lee, J.-R.; Choi, Y.-S.; Yook, J.; Kim, B.-S.; Lee, J.-C. Synthesis and characterization of biocompatible copolymers containing plant-based cardanol and zwitterionic groups for antifouling and bactericidal coating applications. *Eur. Polym. J.* **2019**, *112*, 688-695. DOI: 10.1016/j.eurpolymj.2018.10.034
(46) Zhang, X.; Lin, B.; Zhao, K.; Wei, J.; Guo, J.; Cui, W.; Jiang, S.; Liu, D.; Li, J. A free-standing calcium alginate/polyacrylamide hydrogel nanofiltration membrane with high anti-fouling performance: Preparation and characterization. *Desalination* **2015**, *365*, 234-241. DOI: 10.1016/j.desal.2015.03.015
(47) Xu, X.; Sun, Y.; Zhang, M.; Zhao, R.; Zeng, S.; Xu, Y.; Nie, W.; Zhou, Y.; Chen, P. Boosting the visible-light-driven photocatalytic antibacterial performance of MoS_2 nanosheets by poly (3-(4-methyl-3'-thiophenoxy)) propyltrimethylammonium chloride (PThM) modification. *J. Mater. Chem. B* **2022**, *10* (23), 4405-4415.
(48) Shen, H.; Liao, S.; Jiang, C.; Zhang, J.; Wei, Q.; Ghiladi, R. A.; Wang, Q. In situ grown bacterial cellulose/MoS_2 composites for multi-contaminant wastewater treatment and bacteria inactivation. *Carbohydr. Polym.* **2022**, *277*, 118853.
(49) Zhang, M.; Wang, K.; Zeng, S.; Xu, Y.; Nie, W.; Chen, P.; Zhou, Y. Visible light-induced antibacterial effect of MoS_2: Effect of the synthesis methods. *Chem. Eng. J.* **2021**, *411*, 128517.

(50) Zhao, Y.; Jia, Y.; Xu, J.; Han, L.; He, F.; Jiang, X. The antibacterial activities of MoS_2 nanosheets towards multi-drug resistant bacteria. *Chem. Commun.* **2021**, *57* (24), 2998-3001.
(51) Cheng, H.; Wang, J.; Yang, Y.; Shi, H.; Shi, J.; Jiao, X.; Han, P.; Yao, X.; Chen, W.; Wei, X.; et al. $Ti_3C_2T_X$ MXene Modified with ZnTCPP with Bacteria Capturing Capability and Enhanced Visible Light Photocatalytic Antibacterial Activity. *Small* **2022**, *18* (26), e2200857. DOI: 10.1002/smll.202200857
(52) He, D.; Zhang, Z.; Xing, Y.; Zhou, Y.; Yang, H.; Liu, H.; Qu, J.; Yuan, X.; Guan, J.; Zhang, Y.-n. Black phosphorus/graphitic carbon nitride: A metal-free photocatalyst for "green" photocatalytic bacterial inactivation under visible light. *Chem. Eng. J.* **2020**, *384*. DOI: 10.1016/j.cej.2019.123258
(53) Liu, W.; Zhang, Y.; Zhang, Y.; Dong, A. Black Phosphorus Nanosheets Counteract Bacteria without Causing Antibiotic Resistance. *Chemistry* **2020**, *26* (11), 2478-2485. DOI: 10.1002/chem.201905134
(54) Zhang, L.; Chen, P.; Xu, Y.; Nie, W.; Zhou, Y. Enhanced photo-induced antibacterial application of graphene oxide modified by sodium anthraquinone-2-sulfonate under visible light. *Appl. Catal. B: Environ.* **2020**, *265*. DOI: 10.1016/j.apcatb.2019.118572
(55) Xu, J.; Wang, Z.; Zhu, Y. Highly efficient visible photocatalytic disinfection and degradation performances of microtubular nanoporous g-C_3N_4 via hierarchical construction and defects engineering. *J. Mater. Sci. Technol.* **2020**, *49*, 133-143. DOI: 10.1016/j.jmst.2020.02.024
(56) Yadav, P.; Nishanthi, S. T.; Purohit, B.; Shanavas, A.; Kailasam, K. Metal-free visible light photocatalytic carbon nitride quantum dots as efficient antibacterial agents: An insight study. *Carbon* **2019**, *152*, 587-597. DOI: 10.1016/j.carbon.2019.06.045.

Table of Contents (TOC)